Nanoanalytical identification of siderite dissolution coupled Pb removal mechanisms from oxic and anoxic aqueous solutions

*Lisa C. Füllenbach**[a], *Jeffrey Paulo H. Perez*[b], *Helen M. Freeman*[b,c], *Andrew N. Thomas*[d], *Sathish Mayanna*[b,e], *Julia E. Parker*[f], *Jörg Göttlicher*[g], *Ralph Steininger*[g], *Jörg Radnik*[h], *Liane G. Benning*[b,i], *Eric H. Oelkers**[a,j]

[a]Department of Earth Sciences, University College London, London, WC1E 6BT, United Kingdom. *l.fuellenbach@ucl.ac.uk; *e.oelkers@ucl.ac.uk

[b]GFZ German Research Center for Geosciences, Telegrafenberg, 14473 Potsdam, Germany

[c]School of Chemical and Process Engineering, University of Leeds, Leeds, LS2 9JT, United Kingdom

[d]Department of Applied Geosciences, Karlsruhe Institute of Technology, 76131 Karlsruhe, Germany

[e]Carl Zeiss Microscopy GmbH, 73447 Oberkochen, Germany

[f]Diamond Light Source, Harwell Science and Innovation Campus, Didcot, OX11 0DE, United Kingdom

[g]Karlsruhe Institute of Technology, Institute for Photon Science and Synchrotron Radiation, 76344 Eggenstein-Leopoldshafen, Germany

[h]Federal Institute for Material Research and Testing, 12235 Berlin, Germany

[i]Department of Earth Sciences, Freie Universität Berlin, 12249 Berlin, Germany

[j]GET, CNRS UMR 5563, 14 Avenue Edouard Belin, 3400 Toulouse, France

GRAPHICAL ABSTRACT. Please find the graphic at the end of this manuscript.

ABSTRACT.

Lead(II) is a toxic pollutant often found in metal-contaminated soils and wastewaters. In acidic aqueous environments, Pb(II) is highly mobile. Chemical treatment strategies of such systems therefore often include neutralization agents and metal sorbents. Since metal solubility and the retention potential of sorbents depend on the redox state of the aqueous system, we tested the efficiency of the naturally occurring redox-sensitive ferrous iron carbonate mineral siderite to remove Pb(II) from acidic aqueous solutions in batch experiments under oxic and anoxic conditions over a total of 1008 h. Siderite dissolution led to an increase of reactive solution pH from 3 to 5.3 and 6.9, while 90% and 100% of the initial aqueous Pb(II) (0.48×10^{-3} mol kg^{-1}) were removed from the oxic and anoxic system, respectively. Scanning and transmission electron microscopy (SEM, TEM), combined with X-ray absorption and photoelectron spectroscopy (XAS, XPS) indicated that, under oxic conditions, Pb(II) was consumed by cerussite precipitation and inner-sphere surface complexation to secondary goethite. Under anoxic conditions, Pb(II) was removed by the rapid precipitation of cerussite. This efficient siderite dissolution-coupled sequestration of Pb(II) into more stable solid phases demonstrates this potential method for contaminated water treatment regardless of the redox environment.

KEYWORDS. Siderite – XANES-mapping – EXAFS – Lead carbonate – Iron oxyhydroxides – Adsorption – Wastewater treatment

1. INTRODUCTION

Human use of land and natural resources often leads to surface and groundwater pollution. Divalent lead (Pb(II)) is one of the most toxic and common contaminants introduced to soils and (sub)surface waterbodies from mine tailings[1,2], waste disposal and landfills[3-5], and industrial activities[6], where concentrations can reach up to several thousand mg of Pb(II) per kg of contaminated soils or sediments[7–9]. Studies of lead removal from aqueous solutions have been mainly focused on chemical sorption under oxic and controlled pH conditions to various substrates including aluminum oxides[10,11], clays[12], soils[13,14], calcite[15-17], and ferric iron (oxyhydr)oxides such as goethite[18-20]. Contaminated environments such as stream sediments[21], floodplain soils[7,8] and tailing dam sites[9], which are in consistent contact with water are highly susceptible to redox changes resulting from periodic (e.g., tidal) or seasonal (e.g., heavy rainfall) fluctuations. As the redox state of a polluted aqueous system directly affects the pH and determines the solubility of many metals and sorbents[21-23], it is necessary to understand the redox state of the system to predict accurately both metal retention and release. While acidity of wastewaters, as in acid mine drainage[24], is commonly overcome by the addition of alkaline, often carbonate materials[25,26], the issue of potential redox fluctuations causing metal release in contaminated waterbodies remains a challenge.

The redox sensitive ferrous carbonate siderite ($FeCO_3$) is a potential candidate material for redox-dependent metal remediation. Several studies have investigated siderite as a reductive sorbent for redox sensitive metal(loid)s such as Cr[27-29], As[30,31], and Hg[32]. Under controlled pH and redox conditions these metal(loid)s were reduced and adsorbed to either the siderite surface or, due to coupled redox reactions, to secondary ferric (oxyhydr)oxides. Little attention has been drawn to illuminate the complete reaction pathway between siderite and contaminant over time,

where siderite can act as both dissolution-induced neutralizer and sorbent under either redox condition. Siderite is highly soluble in acidic aqueous solutions[33], and its dissolution leads to aqueous phase neutralization through bicarbonate production. Under oxic conditions, the release and oxidation of Fe(II) from dissolving siderite results in the precipitation of Fe(III) (oxyhydr)oxides[34]. During dissolution under reduced conditions, iron oxidation is suppressed, and aqueous metals can interact with the siderite surfaces and its dissolution products.

To test whether siderite reactivity in acidic aqueous systems is also sufficient to remove less redox-sensitive metals such as Pb in either redox environment over time, and to better understand the mechanisms involved, we have monitored natural siderite dissolution, pH and metal concentrations in initially acidic Pb(II)-bearing aqueous solutions under oxic and anoxic conditions. We used scanning and transmission electron microscopy to investigate the siderite-precipitate interface and the reaction products. Complimentary X-ray absorption and photoelectron spectroscopic analyses, including high-resolution elemental X-ray fluorescence and absorption spectroscopic mapping, allowed localization and determination of Fe(II/III) and Pb(II) speciation and bonding environment. Data acquired from this set of analyses contributes to the evaluation of the metal retention efficiency of siderite as a potential low-cost *in situ* remediation material.

2. MATERIAL AND METHODS

2.1. Materials

Natural macrocrystalline siderite from Peyrebrune Quarry, France[33], was ground in an agate mortar and sieved to a < 63 μm size fraction. The siderite powder was cleaned by repeated rinsing with ethanol after ultrasonication; its surface area was 9.95 m^2 g^{-1}, as determined by BET

multipoint Krypton adsorption (Quantachrome Autosorb-1MP). Powder X-ray diffraction (XRD; PANalytical X'Pert) confirmed the purity of the cleaned siderite powder (> 98%) with minor amounts of fluorite, quartz and traces of calcite and hematite impurities. Inductively coupled plasma optical emission spectroscopy (ICP-OES; Varian 720ES) of the siderite powder revealed contents of 2.43 wt% Mn, 1.27 wt% Ca, and 0.34 wt% Mg, which are likely structural impurities in siderite and minor calcite. Minor and trace contents of 0.74 wt% S, 0.13 wt% K, 0.02 wt% Na, 0.02 wt% Si, 37.3 ppm Cu, and 24.5 ppm Cr also detected in the ground material are likely contributions from mineral impurities (e.g., quartz, trace sulfides).

2.2. Batch Experiments

All chemicals use in the experiments were reagent or analytical grade from Honeywell Fluka and VWR and used as received. All aqueous stock solutions were prepared using ultrapure deionized water (Milli-Q, resistivity ~18 MΩ·cm). The aqueous solutions used in the oxic experiments were prepared under ambient laboratory conditions, whereas those used in the anoxic experiments were prepared inside an CO_2-free anaerobic chamber (97% N_2, 3% H_2; COY Laboratory Products Inc.) using de-oxygenated deionized water that was sparged with argon at ~90 °C for at least 4 h prior to the experiments. For both the oxic and anoxic experiments, the pH of all starting solutions was adjusted to 3.0 ±0.1 by adding 15.5 M HNO_3 and 2.5 M NaOH, and the ionic strength was adjusted to 2-5 $x10^{-3}$ mol kg^{-1} by adding 0.1 M $NaNO_3$. For all lead-bearing solutions, 0.48 $x10^{-3}$ mol kg^{-1} lead(II) nitrate ($Pb(NO_3)_2$) was dissolved into deionized water prior to ionic strength and pH adjustment. The concentrations of lead used in the experiments are based on average concentrations reported in contaminated environments[6-9].

All oxic and anoxic experiments were performed in duplicate in batch reactors that were continuously mixed on a rotary mixer. A list of all experimental details is provided in Table S1. For each experiment, based on preliminary experiments (not shown) and studies using siderite as metal sorbent[27,29,30], 6 g L^{-1} siderite was reacted with the oxic and anoxic acidic Pb(II)-bearing aqueous solutions. Control experiments in the absence of Pb were also conducted following the same procedures (Figure S1). To allow the analysis of the fluid and the solid phases at various stages of the siderite dissolution reaction, a series of 15 distinct single short-term (ST) batch experiments were performed and ended at different times. The experiments in these series ran for 0.5, 1, 2, 3, 6, 12, 20, 28, 36, 48, 60, 72, 96, 144, and 240 h. Additional long-term (LT) experiments were run for a total of 1008 h; during these experiments, fluid aliquots were collected every 168 h. Sampling of liquid aliquots from the oxic experiment was conducted within minutes to avoid equilibration of the reactive fluid with atmospheric CO_2. Final solids and fluids from all experiments were separated for analysis by vacuum filtration using 0.2-µm nylon filters. To avoid potential iron oxidation and to ensure all iron remained dissolved in the filtrates, aliquots were immediately acidified after. The collected solid residues were kept dry or in ethanol at ambient conditions, and in case of the anoxic samples in the anaerobic chamber, to prevent further phase transformation.

The elemental concentrations of all 214 collected fluid samples were measured using ICP-OES (Varian 720ES / Agilent Technologies 5110); the average relative standard deviation (RSD) of the analyses ranged from 0.3 to 1.2% (Table S2). Final liquid samples with Pb concentrations below the detection limit of the ICP-OES were remeasured using the more sensitive inductively coupled plasma mass spectrometer (ICP-MS; Bruker 90); analyses were within an accuracy of 0.57% RSD. To determine the oxidation of dissolved Fe^{2+} to Fe^{3+} in the reacted aqueous solutions, Fe speciation

was measured by the colorimetric Ferrozine method[35] using a segmented flow analysis device (SFA; SEAL AutoAnalyzer 3HR) equipped with a digital colorimeter. The average RSD of these measurements ranged between 0.34 and 0.35%. Comparison of the total iron concentrations determined using SFA (Fe^{total}_{SFA}) to those obtained by ICP-OES (Fe^{total}_{OES}) revealed that $Fe^{total}_{SFA} \approx Fe^{total}_{OES}$, whereupon Fe^{total}_{OES} is a close approximation of the Fe^{2+} released during siderite dissolution (Figure S2).

2.3. Solid phase characterization

Initial and reacted siderite and selected secondary solid reaction products were imaged and analyzed using a ZEISS Ultra Plus Gemini field-emission scanning electron microscope (FE-SEM) equipped with an In-lens secondary electron and UltraDry SDD energy dispersive X-ray (EDX) detectors. Solids collected from anoxic experiments were mounted onto SEM stubs inside the anaerobic chamber and transported to the SEM facility using an anaerobic jar to avoid sample oxidation.

Bulk mineral structure analyses were performed with a high resolution PANalytical X'pert PRO MPD diffractometer equipped with a Co anode X-ray tube (λ = 1.789 Å), a Ge incident beam monochromator and a X'celerator detector. Repeated measurements of anoxic samples stored under dry ambient laboratory conditions for 19 h and 5 weeks verified the long-term stability of siderite and secondary phases.

High resolution morphological and structural analyses were performed with a FEI Tecnai G2 F20 X-Twin transmission electron microscope (TEM) operated at 200 kV with a Schottky field emitter as an electron source. The TEM is equipped with a Gatan Imaging Filter (Tridiem™) and a Fishione high-angle angular dark-field detector (HAADF) and an EDAX X-ray analyzer for

simultaneous elemental analysis. Combined fast Fourier transform (FFT) was used to determine local structure and morphology of the secondary particles.

X-ray absorption near edge spectroscopy (XANES) combined with X-ray fluorescence (XRF) mapping at beamline I14 of the Diamond Light Source (UK) was used on the oxic sample to determine the elemental distribution of Fe and Pb and to identify the speciation and oxidation state of Fe and Pb in the metal-binding phases. The Python-based software ATHENA[36] and MANTIS were used for data processing. Complimentary extended X-ray absorption fine structure (EXAFS) spectra were collected at the ANKA-KIT synchrotron (Germany) SUL-X beamline to investigate the local bonding environment of Pb in both oxic and anoxic samples. Data reduction was performed using ARTEMIS software[36]. Details on the fitting procedures of XANES and EXAFS data are given in the Supplementary Information. Pure mineral model compounds were used to fit the XAS data; Pb(II)-adsorbed ferrihydrite was used as representative for Pb(II) adsorption to ferric oxyhydroxide surfaces. The high carbonate solubility and reactivity of siderite, impeded the preparation of Pb(II)-adsorbed siderite as model.

The surface chemistry of the anoxic samples was investigated by X-ray photoelectron spectroscopy (XPS) to determine Pb speciation on the siderite surfaces using a KRATOS Axis Ultra DLD. Data reduction was performed using UNIFIT software[37].

2.4. Geochemical Modelling

Saturation indices of the phases involved in this study were calculated based on measured aqueous solution chemistry data using the software PHREEQC[38] together with its 2017 Lawrence Livermore National Library database.

3. RESULTS

3.1. Pb(II) uptake during siderite dissolution

In Pb(II)-bearing oxic aqueous solutions, the pH reached 4.5 within 2-3 h of reaction and continued to increase steadily to a final pH of 5.3 (Figure 1A). Simultaneously, Fe^{total} concentrations increased to 0.14 $x10^{-3}$ mol kg^{-1} during the first 2-4 h of reaction. A subsequent distinct drop in aqueous Fe^{total} concentrations and a visible change in the color of the suspension to reddish ochre indicated the precipitation of ferric (oxyhydr)oxides; the onset of ferrous iron oxidation and ferric oxyhydroxide precipitation may have initiated as soon as pH 4 was reached[39]. Within 2 h after the onset of siderite dissolution, 9 ±3.6% of the initial aqueous Pb(II) was removed from the aqueous solution; after 1008 h 90% of the Pb(II) was removed (Figure 1C). Under anoxic conditions, the pH of the Pb(II)-bearing aqueous solution increased to 5.1 within 0.5 h and to 6.5 after 96 h of reaction; from this time onwards, the pH increased steadily to 6.9 at the end of the experiment (Figure 1B). The Fe^{total} concentrations peaked at 0.36 $x10^{-3}$ mol kg^{-1} after 168 h of reaction. Notably, Pb(II) was completely removed from the aqueous solution within 96-144 h of reaction (Figure 1D). The final aqueous Pb(II) concentrations were < 10 µg L^{-1}, the upper limit of Pb(II) allowed in drinking water by the EU ECD[40], which demonstrates the Pb(II) removal efficiency of this method.

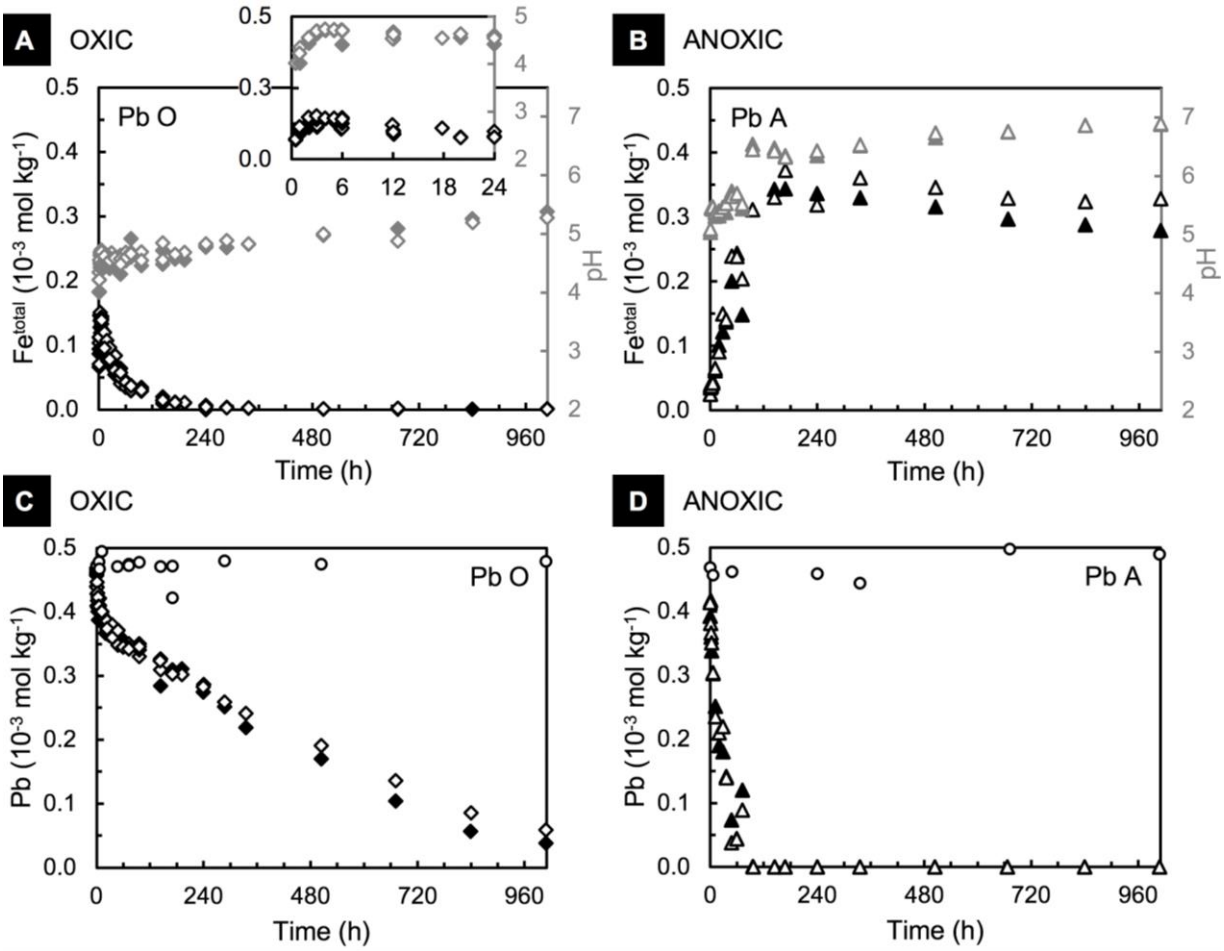

171 **Figure 1.** Total metal concentrations (black symbols) and pH (grey symbols) shown as a function of time. Fe^{total} and
172 pH during siderite dissolution in the presence of Pb(II) under oxic (**A**; diamonds) and anoxic conditions (**B**; triangles);
173 corresponding Pb(II) concentrations are given in **C** and **D**, respectively (circles = control solutions). Error bars are
174 smaller than the symbols. Standard error of the pH probe is ±0.01, RSD% (ICP-OES) is 0.29 to 1.23%. Shown are
175 data from all Pb(II)-bearing experiments (Table S1). For clarity, Fe^{total} concentrations and pH measured during the
176 first 24 h of the oxic experiment are shown in the inset in **A**.

177

178 **3.2. Characterization of the reaction products**

179 The solids recovered from the oxic and anoxic Pb(II)-bearing aqueous solutions after 1008 h
180 were characterized using SEM imaging combined with EDX analyses, TEM and XRD. An
181 overview of the XRD results is given in Figure S3 and Table S3. Measured *d*-spacings from TEM
182 images and their corresponding FFT patterns are compiled in Table S4.

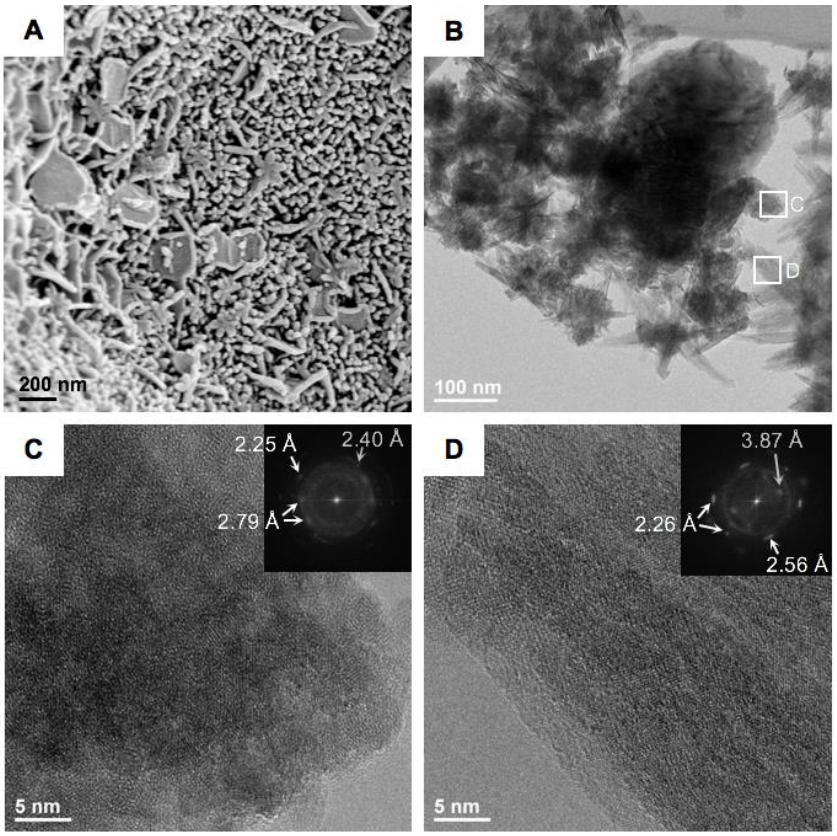

Figure 2. Scanning and transmission electron micrographs of siderite reacted in Pb(II)-bearing solutions for 1008 h under oxic conditions (Pb O LT). **A** Rod-shaped and intercalated pseudo-hexagonal tabular precipitates covering a siderite surface. **B** Ultra-fine precipitates collected from the reactor suspension: a nearly completely reacted siderite fragment overgrown and surrounded by nanoparticulate precipitates forming clumps (**C**) and rods (**D**) via (nearly) oriented attachment; respective FFT patterns of the nanoparticles are indicative of goethite **(**2.25-2.26 Å, 2.56 Å), traces of hematite (3.87 Å) and residual siderite (2.40 Å, 2.79 Å). See Table S4 for measured *d*-spacings and reference data.

After 1008 h of reaction under oxic conditions, the recovered siderite grains were heterogeneously covered with secondary phases identified as nanoparticulate goethite (α-FeOOH) (Figure 2). Minor amounts of hematite (α-Fe_2O_3) were also present in the unreacted siderite starting material and are thus not considered a reaction product. The precipitates formed a discontinuous layer of ≤ 100-200 nm rods and needles randomly oriented to the siderite surface, partially radially intergrown and occasionally intercalated with tabular crystallites (Figure 2A).

Ultra-fine precipitates collected from the reacted suspension consisted of ca. 5 nm long nanoparticles forming aggregates of ≤ 100 nm clumps with 100-200 nm long rods growing out of the clumps (Figure 2B). The lattice spacings in the clumped nanoparticles measured 2.25 Å (Figure 2C), and 2.56 Å in the rods (Figure 2D), identifying both precipitates as goethite. Faint spots in the FFT patterns (insets Figure 2C and 2D) from the particle aggregates, exhibited lattice spacings of 2.40 and 2.79 Å, which suggest the presence of residual siderite, and of 3.87 Å which suggests traces of hematite.

Siderite reacted with aqueous Pb(II) under anoxic conditions resulted in the precipitation of ≤ 5 µm rounded particles and micron-scale aggregates on the smooth but etched siderite surfaces (Figure 3A). EDX analyses of the reacted siderite grains, their surfaces and the precipitates showed enrichment of Pb (Figure 3B; Figure S4). XRD analyses identified nanocrystalline cerussite ($PbCO_3$) as the secondary phase (Figure S3). This was confirmed by TEM imaging and FFT analyses of the polycrystalline material attached to the siderite surfaces exhibiting *d*-spacings of 2.17 Å, 2.63 Å and 2.92 Å, which are characteristic for cerussite (Figure 3C), while lattice spacings of 1.53 Å likely resulted from the presence of nearby siderite. No residual hematite from the unreacted material was found in the reacted solids, suggesting Fe(II)-induced reductive dissolution of this ferric component[41-43]. Notably, within the top 20 nm of a reacted siderite, a reaction zone was observed exhibiting a poorly (poly)crystalline phase oriented in a seemingly random angle to the underlying siderite. The lattice spacings of this phase matched that of the cerussite (Figure 3D-E).

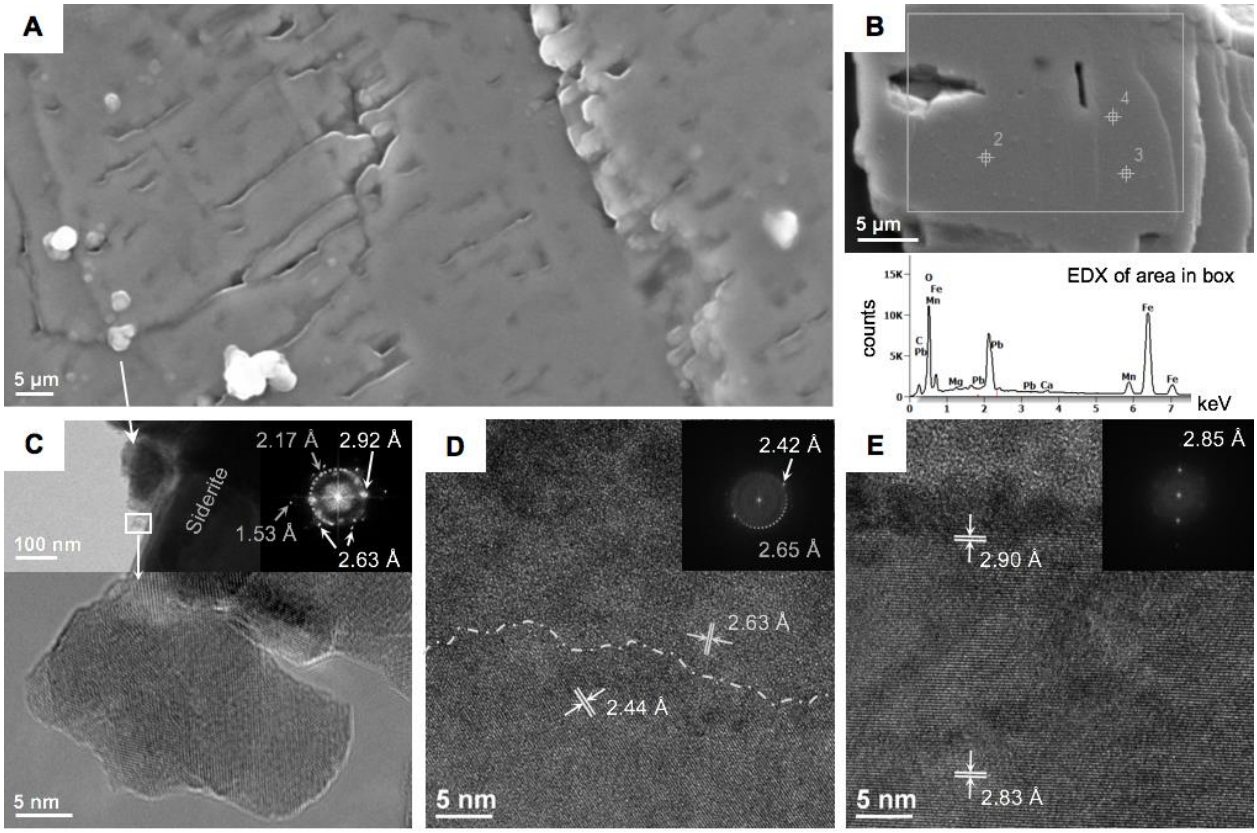

Figure 3. Scanning and transmission electron micrographs of siderite reacted in Pb(II)-bearing aqueous solutions for 1008 h under anoxic conditions (Pb A LT). **A** Reacted siderite grains showing dissolution-features, micron-scale precipitates and Pb-enrichment on the surface (**B**). **C** TEM and the respective FFT pattern identify the precipitates as cerussite (2.63 Å, 2.92 Å) attached to siderite (1.53 Å, 2.17 Å). **D** Structurally independent cerussite (2.63-2.65 Å) growth on the reacted siderite surface (2.44 Å). **E** Widening of the siderite crystal lattice (2.83 Å) near the reacted surface to *d*-spacings indicative for cerussite (2.90 Å). See Table S4 for measured *d*-spacings and reference data.

3.3. Speciation and local bonding environment of Pb

A set of complimentary XAS and XPS analyses were performed to determine the bonding environment of Pb associated with the solids recovered from the oxic and anoxic experiments. Results are presented in Figures 4, 5, and S5; respective fitting parameters are given in Tables 1, 2, and S5.

230 *3.3.1. Pb speciation and bonding in the oxic system*

231 Linear combination fitting (LCF) results of the Fe K-edge XANES spectra obtained from the
232 bulk solid sample of the oxic experiment indicated that ca. 5% of the reacted solid-bound iron
233 Fe(II) oxidized to Fe(III) during siderite dissolution in the presence of Pb(II) (Table 1). XRF
234 elemental mapping of individual reacted siderite grains showed that Pb was present on all analyzed
235 siderite surfaces, however, relatively higher concentrations were occasionally observed along the
236 edges, while lower Pb concentrations were detected on (fracture) planes (Figure 4D-G). High-
237 resolution XANES mapping of selected areas on grain surfaces showed that in areas of increased
238 Pb concentrations, 83-85% of Fe was present as Fe(III). In areas with lower Pb concentrations,
239 79% of solid-bound Fe had remained as Fe(II) (Figure 4C). This Fe(II)-Fe(III) distribution on the
240 reacted siderite surfaces indicates heterogeneous surface oxidation and/or covering with secondary
241 ferric precipitates. Notably, LCF results of the Pb L_{III}-edge spectra of the same mapping area did
242 not indicate a spatial correlation with or preference of Pb for either iron oxidation state. In contrast,
243 39% of the solid-associated Pb was oxide-bound, and 61% was present as Pb carbonate (Figure
244 4F, area 1). In a mapped area of another grain of reacted siderite, the XRF element map indicated
245 an equal distribution of Pb and a predominance of Fe(III) in the XANES map (Figure 4G, area 2).
246 The LCF of the Pb L_{III}-near edge spectrum of this area, however, indicated a higher contribution
247 of oxide-bound Pb over Pb carbonate (Figure 4B, area 2).

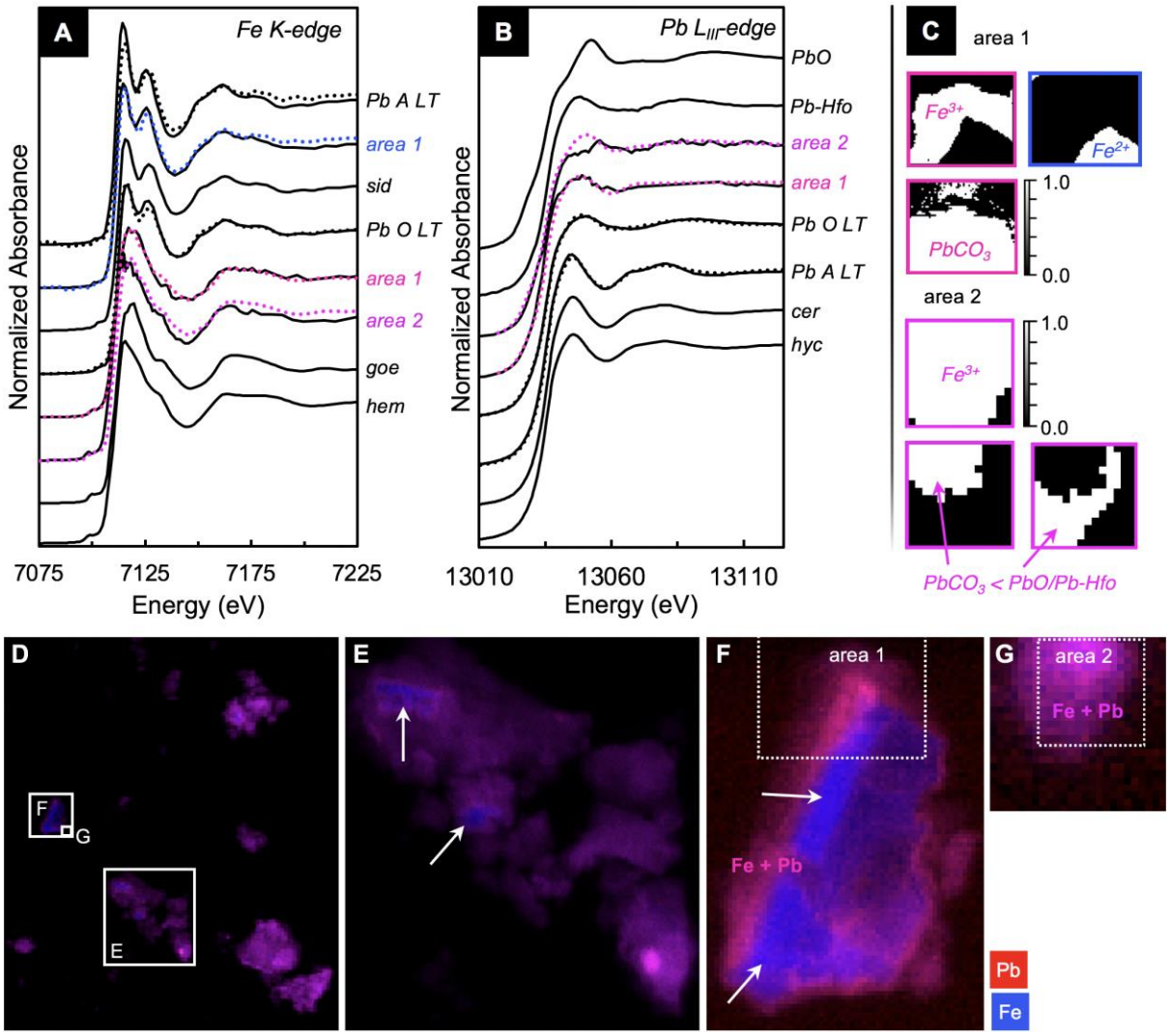

Figure 4. XANES spectra of model compounds and reacted siderite in the presence of aqueous Pb(II) under oxic and anoxic conditions after 1008 h of reaction. **A** Fe K-edge of samples and standards. **B** Pb L_{III}-edge of samples and standards. Pb A LT = anoxic long-term experiment, Pb O LT = oxic long-term experiment; sid = siderite, goe = goethite, hem = hematite, PbO = massicot (orthorhombic); Pb-Hfo = Pb-adsorbed hydrous ferric oxide (ferrihydrite), cer = cerussite, hyc = hydrocerussite. Black lines represent bulk sample analyses. Dotted lines represent linear combination fits; colored lines correspond to high-resolution XANES mapping areas (**C**) in **F** (area 1; 6.5 x 5.5 µm) and **G** (area 2; 1.5 x 1.5 µm) mapped at a 100 x 100 nm pixel size. Note that in all XANES spectra are mixtures of Fe and Pb bonding environments, respectively (see Table 1); the dominant species are indicated in **C**. **D-G** High-resolution X-ray fluorescence maps of reacted siderite grains reacted in Pb(II)-bearing aqueous solution under oxic conditions (Pb O LT); white outlines indicate magnified areas shown in **E-G**. Red = Pb, blue = Fe, magenta = Fe + Pb. Note that the Pb distribution varies only slightly and locally; strongly blue (Fe-rich) areas possibly indicate precipitate-free surfaces or fracture planes (white arrows). Image dimensions: **D** = 165 x 145 µm, **E** = 45 x 38 µm, **F** = 18 x 13 µm, **G** = 2.5 x 2.5 µm.

Table 1. XANES Fe K-edge and Pb L_{III}-edge linear combination fitting parameters and speciation of solids collected from both oxic[a] and anoxic[b] long-term experiments measured in bulk and at high resolution mapping. Area 1 measured 6.5 x 5.5 µm (Figure 4F), area 2 covered 1.5 x 1.5 µm (see Figure 4G).

Edge	Sample	χ^2	$\chi^2_{reduced}$	Standard material*			*Error* ±(%)
				Pb-adsorbed	Oxide	Carbonate	
Fe *K*-edge					**Fe_2O_3** *(Fe^{3+})*	**$FeCO_3$** *(Fe^{2+})*	
Pb O LTa	*bulk*	0.04	0.0006		4.9	95.1	3.1
	area 1†	0.93	0.0095		83.1	16.9	9.0
	area 1†	0.07	0.0013		20.8	79.2	4.5
	area 2‡	0.04	0.0007		85.1	14.9	3.4
Pb A LT[b]	*bulk*	0.27	0.0040		–	100.00	0.0
Pb *L_{III}*-edge				**Pb-Hfo**[c]	**PbO**	**$PbCO_3$**	
Pb O LT	*bulk*	0.01	0.0001	55.9[d]	25.4[d]	18.7	2.0
	area 1†	0.03	0.0008	–[d]	38.6	61.4	5.2
	area 2‡	0.06	0.0012	19.0	54.4	26.6	1.8
Pb A LT	*bulk*	0.02	0.0001	–	–	100.0	3.6

*Fit results normalized to 100%; †see Figure 4C and F; ‡see Figure 4C and G;
[a] Oxic, [b] anoxic long-term experiment; see Table S1 for experimental specifications.
[c] Hfo = hydrous ferric oxide (ferrihydrite). [d] Fits using only Pb-Hfo and no PbO resulted in poorer fit statistics.

Shell-by-shell fits of the Pb L_{III}-edge EXAFS region of the solids indicate a first shell Pb–O interatomic distance R of $R_{Pb\text{-}O}$ = 2.31 Å; this distance is indicative of Pb(II) adsorbed to iron (oxyhydr)oxides (Table 2). Previous studies reported radial distances of $R_{Pb\text{-}O} \leq 2.35$ Å for a distorted trigonal pyramidal coordination of Pb with the surface oxygen of goethite[44-47]. A second single scattering path of $R_{Pb\text{-}Fe}$ = 3.31 Å falls within the reported range of $R_{Pb\text{-}Fe}$ distances of 2.91-3.49 Å, indicative of the bidentate mononuclear inner-sphere surface complexation with FeO_6-octahedra in the iron (oxyhydr)oxide surface[44]. The coordination number of this pathway is similar (0.55) to values observed in previous EXAFS studies of Pb adsorbed on Fe(III) oxyhydroxide surfaces[20] and lies within the range of values expected for a bidentate mononuclear surface complex (≤ 1.0). In contrast to the clear indication of Pb-carbonate environments in the XANES

spectra, the EXAFS data lack unambiguous evidence of carbon scattering. Reasons for this may be a combination of methodologic limitations and sample specifics. Since carbon is a weak backscattering atom and lead is a strong absorber, the contribution of the Pb–C scattering with $R_{Pb–C} \geq 3.5$ Å to the EXAFS spectrum[20] may be insignificant in poorly crystalline materials such as the reacted siderite surface and Pb surface complexes[48]. The wide but discontinuous coverage of siderite grain surfaces with precipitates observed in SEM imaging, and the continuous presence of Pb-carbonate species indicated in XANES mapping (Figure 4), suggest that Pb is also associated with carbonate at the siderite surface. It seems likely, therefore, that the observed contributions of Pb–C scatterings to the EXAFS spectrum of the bulk sample were overshadowed by the more prominent Pb–Fe scattering of Pb.

Table 2. EXAFS Pb L_{III}-edge k^3-weighed shell fitting parameters and interatomic path lengths measured on bulk solid samples from both oxic[a] and anoxic[b] long-term experiments. Uncertainties are given in brackets.

	ΔE_0 (eV)	R-range (Å)	**Shell**	**N**	**R** (Å)	**σ^2** (Å^2)
Pb O LT[a]	-6.7 (2.1)	1.2 – 4.0	Pb–O	2.24 (0.17)	2.31 (0.03)	0.01*
			Pb–Fe	0.55 (0.25)	3.31 (0.02)	0.01*
Pb A LT[b]	-0.05 (3.5)	1.5 – 5.0	Pb–O	8.4 (2.91)	2.65 (-0.02)	0.027 (0.006)
			Pb–C	3*	3.15 (0.07)	0.027 (0.006)
			Pb–Pb	6*	4.15 (-0.07)	0.014 (0.004)

* Parameter was set during fitting.
ΔE_0 = energy shift. N = coordination number (degeneracy). R = interatomic path lengths. σ^2 = Debye-Waller disorder term. The amplitude reduction factor (S_0^2) was set to 0.9 in all fits.

3.3.2. Pb speciation and bonding in the anoxic system

XANES Fe K-edge spectra of the bulk solids collected from the anoxic experiments confirmed that Fe(II) oxidation did not occur and all solid-bound Fe(II) remained as carbonate (Figure 4A). LCF of the respective Pb L_{III}-edge spectra indicate that 100 ±3.6% of the solid-bound Pb(II) was

present as carbonate (Table 1). In the EXAFS Pb L_{III}-edge shell fitting, the spectrum could be closely fit to cerussite with physically reasonable deviations from the ideal structure indicating that Pb is present in a 9-fold coordination[49] (Table 2).

Additional XPS analyses of the anoxic sample (Table S5) showed Pb $4f_{7/2}$ and $4f_{5/2}$ peaks at binding energies of 138.6 and 143.5 eV, respectively. These agree well with the binding energies reported for Pb(II) in Pb-carbonates[50,51], Pb-calcite[15] and Pb-aragonite[52] (Figure 5). Shifts towards higher binding energies by 0.3 and 0.4 eV observed in the O 1s and C 1s spectra of the reacted sample indicative for $MeCO_3$[53,54] suggest a change from the calcite-type into the aragonite-type carbonate structure[52].

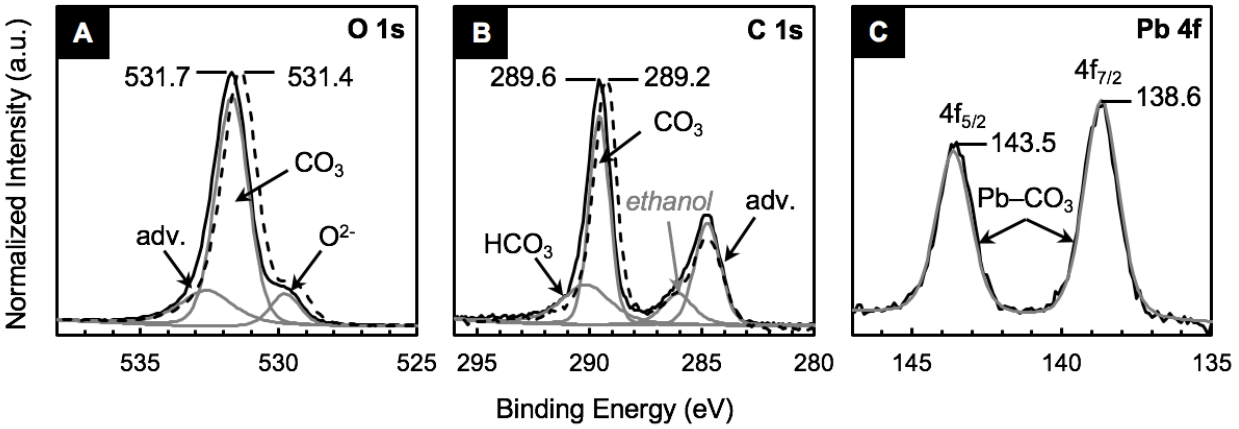

Figure 5. XPS spectra of the (**A**) O 1s, (**B**) C 1s and (**C**) Pb 4f photoelectron lines obtained from the siderite sample reacted with aqueous Pb(II) for 1008 h under anoxic conditions (Pb A LT) shown as solid black curves; spectra obtained from the unreacted siderite sample are shown for comparison in dashed curves. Grey curves show the best fits of the spectra of the reacted sample. Adv. = adventitious carbon. Shifts in the O 1s and C 1s spectra of the reacted sample relative to the unreacted siderite samples toward higher energies by 0.3 and 0.4 eV, respectively, indicate a change in the carbonate structure, possibly due to recrystallization from siderite to cerussite on the reacted siderite surface[52]. The ethanol detected in the C 1s spectra originates from sample storage in ethanol.

4. DISCUSSION

4.1. Reaction mechanisms of Pb(II) removal during siderite dissolution

Siderite dissolves readily in acidic aqueous solution, with its solubility decreasing with increasing pH[34,55]. Its reaction products differ strongly under different redox conditions due to the redox sensitivity of the ferrous iron released into the reactive solution, which influences the mechanisms of Pb(II) removal from the reactive solution.

4.1.1. Siderite dissolution coupled iron oxidation and goethite precipitation

During siderite dissolution under oxic conditions, the released ferrous iron oxidizes and precipitates as goethite nanoparticles after > 2 h of reaction at a pH of ≥ 4.5 consistent with the reaction

$$FeCO_3(s) + ½\ O_2 + H_2O \rightarrow \alpha\text{-}FeOOH(s) + HCO_3^- \qquad \text{(eq. 1)}.$$

Note that the aqueous solution pH continuously increased during the experiment. This suggests that proton-consuming siderite dissolution dominates over proton-releasing reactions of iron oxidation, precipitation and adsorption during the oxic experiments. TEM and SEM imaging showed heterogeneously distributed precipitates particularly growing along crystal edges, and nanorods growing from the siderite surface at random orientations. Similar observations were reported by Renard et al.[56], showing interface-coupled siderite dissolution and structurally independent secondary ferric iron phase precipitation. Structurally independent discontinuous precipitation suggests heterogeneous nucleation and growth on the siderite surface, arising from the structural dissimilarity between the dissolving trigonal parent material siderite and the orthorhombic goethite precipitate[57]. Such coatings contain pores allowing the reactive fluid to

continuously dissolve the substrate without affecting the dissolution rate (Figure S6 and Table S6); a similar process has been suggested for otavite (Cd-carbonate) precipitation on aragonite[58]. There was no evidence for potentially dissolved atmospheric CO_2(g) enhancing siderite dissolution upon exposure to air during sampling. As the aqueous solution pH was less than 6, such effects would be insignificant[59].

4.1.2. Coupled siderite dissolution and cerussite precipitation

Under both oxic and anoxic conditions, initial aqueous Pb(II) concentrations decreased with the onset of siderite dissolution. Under oxic conditions, ca. 9% of Pb(II) was removed from solution during the first 2 h of reaction, before the visible precipitation of goethite. Within the first 0.5 h of reaction under anoxic conditions, ca. 13% Pb(II) was removed from solution. Complementary PHREEQC calculations based on the measured aqueous solution composition indicate that both oxic and anoxic Pb(II)-bearing aqueous solutions were saturated with respect to cerussite within less than 0.5 h of reaction, and thus shortly after the onset of siderite dissolution (Table S7). Since cerussite is markedly less soluble (log K_{sp} = -13.2)[60,61] than siderite (log K_{sp} = -10.9)[33] under the investigated experimental conditions, Pb(II) preferentially precipitated as cerussite as soon as sufficient aqueous carbonate was available from siderite dissolution regardless the redox condition of the reactive solution.

Under oxic conditions, early siderite dissolution-induced cerussite precipitation may explain the Pb-carbonate scattering contributions of up to ca. 19% in bulk and locally up to ca. 60% of the solid-bound Pb(II) in the XANES spectra. The tabular crystallites observed in SEM images growing from the siderite surface of the solids collected from the oxic experiments after 2-72 h of reaction, and the pseudo-hexagonal tabular crystallites observed among the surface layer of

352 goethite formed by the end of the experiment (Figure S7) resemble cerussite precipitates formed
353 on aragonite surface reported by Godelitsas et al.[52]. Similar crystallites were also observed in the
354 solids recovered from the anoxic experiments, but were absent, however, in the solids collected
355 from the Pb(II)-free experiments (Figure S8). These observations confirm cerussite formation
356 under both redox conditions despite the lack of evidence for cerussite in the XRD analysis of the
357 oxic sample, in which the minor quantities of cerussite formed were most likely overshadowed by
358 the secondary goethite in this sample.

359 Under anoxic conditions, XRD, XPS and XANES analyses confirmed crystalline cerussite
360 formation and that 100% of the Pb is bound as a carbonate at the end of the long-term experiment.
361 Our TEM data of the reacted siderite suggest local changes of its near-surface structure. A 20 nm
362 thick surface reaction zone, exhibiting a widening of the siderite lattice and overgrowths of poorly
363 (poly)crystalline material were observed, with both features exhibiting lattice distances indicative
364 of cerussite (Figure 3D-E). Pb(II) has an ionic radius of 1.19 Å in octahedral coordination, and an
365 ionic radius of 1.35 Å in the 9-fold coordination as in cerussite[49,62]. These Pb(II) radii are 53% and
366 75% larger than the radius of octahedrally coordinated Fe(II) in siderite (0.780 Å)[62,63].
367 Incorporation of Pb(II) into the dissolution-induced vacated FeO_6 site in siderite would thus lead
368 to distortion and a marked widening of the siderite lattice, despite possible relaxation of the siderite
369 surface structure due to dissolution. Although the relatively large Pb(II) and Ba(II) ions have been
370 reported to incorporate into the $^{[6]}$Ca(II) site in calcite[64,65], dilation around potentially incorporated
371 Pb(II) ions into the much smaller $^{[6]}$Fe(II) site in siderite is expected to be much more significant
372 than that observed for the incorporation of Pb(II) and Ba(II) into the larger metal site of Ca(II) (1.0
373 Å)[62] in calcite[64]. EXAFS shell fitting, however, clearly indicates the 9-fold coordination of Pb(II)
374 in cerussite. The shift towards higher binding energies in the O and C 1s spectra further imply non-

isotype mineral replacement. Although studies of Pb(II) sorption to calcite at pH 8.3 reported no evidence of Pb incorporation or solid solution formation[17], slight variations in the initial Pb(II) concentrations and pH conditions can lead to the (co)precipitation of Pb-carbonates[66,67]. Similar studies of $CaCO_3$ interaction with Pb and transition metals at pH 2.8 to 7 showed dissolution-induced (co)precipitation of divalent metal carbonates[52,58,68-72]. While the replacement of orthorhombic aragonite by isotypic cerussite is fast and results in an epitaxial layer[52,72], the replacement of trigonal siderite by orthorhombic cerussite requires a structural change. Solvent-mediated transformation of non-isostructural carbonates show random orientation of the precipitate relative to its host substrate[69,71,72], similar to what was observed in TEM analyses (Figure 3D). Therefore, a coupled process of dissolution and re-precipitation-controlled transformation as shown by Yuan et al.[71] and Di Lorenzo et al.[72] for the structurally independent replacement of trigonal calcite by orthorhombic cerussite likely explains the observed changes in surface structure and mineral phase. This was likely facilitated by micro-pore generation due to the differences in structure, solubility and molar volume between siderite and cerussite[58,71,72].

4.1.3. Pb(II) adsorption to goethite and siderite

Under oxic conditions, the continued precipitation of goethite over time led to a wide, discontinuous coverage of the siderite surfaces and to the growth of these precipitates in the reactive fluid suspension through aggregation (Figure 2A-B; Figure S7). Shell-by-shell fitting of the Pb L_{III}-edge EXAFS spectra of the bulk solid reaction products indicated interatomic distances of $R_{Pb\text{-}O}$ = 2.31 Å and $R_{Pb\text{-}Fe}$ = 3.31 Å in the first and second coordination shell, respectively (Table 2). Both interatomic distances are in perfect agreement with distances reported for Pb-adsorbed to goethite[47] and characteristic for inner-sphere bidentate edge-sharing Pb(II)-adsorption to iron (oxyhydr)oxides[44-47]. This conclusion is supported by the XANES spectra of the bulk sample and

area 2 (Figure 4). LC fits indicate a distorted trigonal pyramidal coordination of Pb(II) with surface oxygens characteristic for Pb(II) adsorbed to ferric (oxyhydr)oxides[44]. Some of the scattering contributions also indicate a distorted tetragonal pyramidal coordination of Pb(II) as in PbO (orthorhombic)[73,74], which implies the presence of an additional oxygen atom in the distorted adsorption coordination sphere. This may be supported by the first shell Pb–O distance, which is slightly longer than for a trigonal sorption geometry ($R_{Pb\text{-}O}$ ~2.25–2.28 Å)[44,74]. Contributions of these scatterings are particularly prominent in the locally resolved XANES mapping spectra and potentially result from dehydration and enclosure of Pb(II) ions during advanced aggregation and growth of the iron oxyhydroxide surface precipitates on the reacted siderite grains. The absence of second-neighbor oxygens and the low coordination number suggest that Pb(II) is adsorbed rather than incorporated[47,74]. Also, the absence of third shell scatterings exclude ternary absorption of carbonate[20]; in contrast, the first-shell sensitive XANES spectrum suggests the Pb-carbonate coordination of cerussite.

Since at least ca. 9% of the initial Pb(II) concentrations in the reactive aqueous solution was likely consumed by cerussite formation preceding goethite precipitation, the majority of remaining carbonate-bound Pb(II) was likely consumed by the growth of the cerussite precipitates to ≥ 100 nm large crystallites (Figure 2A, Figure S7) until the reactive aqueous solution reached equilibrium with respect to cerussite after approximately 500-600 h of reaction and a pH of 5.0 (Figure 1; Table S7). However, the early sorption of Pb(II) to siderite, as reported to occur within 30 min under acidic pH conditions[75], cannot be ruled out. Bivalent metal carbonates $MeCO_3$ (with Me = Ca, Fe, Mn) generally exhibit a high affinity to sorb heavy metals such as Zn(II), Cd(II) and Pb(II) to their surfaces[15-17,53,66-68,75,76]. For siderite, the pH of neutral surface charge (pH_{PZC}; point of zero charge) is 5.3 ±0.1[77]. At pH < pH_{PZC} carbonate mineral surfaces exposed to aqueous solution adsorb

protons[77]; in the presence of dissolved divalent metals, these can compete with protons for the carbonate surface sites, contributing to the development of a more positive surface charge below the pH_{PZC}[78]. This suggests that Pb(II) could also have sorbed to siderite early in our experiments, forming $>CO_3Pb^+$ surface complexes[77,78], preceding precipitation and growth of cerussite on the siderite surface. Therefore, Pb(II) uptake from the oxic system was likely three-fold: (I) potential sorption to siderite, (II) precipitation as cerussite, and (III) adsorption to goethite. As siderite surface coverage by goethite precipitates advanced over time, and the siderite dissolution rate significantly decreases at a $pH \geq 5$,[34] the adsorption to goethite likely dominated the drawdown of aqueous Pb(II) toward the end of these experiments.

4.2. Environmental implications

In nature, the redox conditions of metal-contaminated sites may not be constant over time, potentially causing sorbed metals to be released[14,21]. Siderite, however, can effectively remove and sustainably retain toxic Pb(II) by precipitation in cerussite from acidic aqueous solutions at varying redox conditions, with no additional harm to the environment. Under either oxygenated or reduced conditions, Pb(II) uptake is governed by siderite dissolution, which is accompanied by rapid increase in pH to less acidic conditions. Initially, some Pb(II) rapidly precipitated as cerussite under either redox condition, followed by its simultaneous sorption onto oxidation-induced goethite nanoprecipitates under oxic conditions, or further precipitation as cerussite under anoxic conditions.

Both mechanisms generate products that are stable under the investigated experimental and comparable natural conditions. Potentially, these dissolution-coupled mechanisms complementarily ensure Pb(II) retention in systems undergoing redox fluctuations, such as

443 contaminated soils, floodplains, or stream sediments. For example, goethite as the reaction product
444 of the oxic experiment is very insoluble under oxic conditions (log K_{sp} = -39.80)[79]. If, however,
445 redox conditions change from oxic to anoxic, reductive dissolution of goethite may occur[23,41-43,80].
446 As a result, the strong inner-sphere complexes of Pb(II) with the goethite surface may become
447 unstable and susceptible to desorption[11,18]. Under reduced and acidic conditions, however, Pb(II)
448 readily precipitates as sparingly soluble cerussite. Since the solubility product of cerussite is
449 substantially lower than that of siderite, Pb(II) is much less susceptible to be liberated from
450 cerussite. Redox sensitivity of carbonate-bound Pb(II) is also negligible compared to Fe(III)
451 (oxyhydr)oxide adsorbed Pb(II). Notably, when Pb(II) was completely consumed by $PbCO_3$
452 formation within 96-144 h of the anoxic experiment, no release of Pb(II) was observed over the
453 remaining experiment duration of > 850 h. This is because of the low solubility and high stability
454 of cerussite over a wide range of pH conditions[60,81], inhibiting Pb remobilization. In turn, the
455 oxygenation of the $FeCO_3$–Pb/$PbCO_3$–H_2O system would provoke goethite precipitation and
456 Pb(II) adsorption to goethite. The observed aggregation of the nanoparticulate goethite may
457 additionally promote Pb(II) retention in the oxic system[82,83]. Elevated pCO_2(g) at above neutral
458 pH, as often present in soil fluids or carbonate-rich surface waters, may enhance Pb(II) retention
459 by enhanced siderite dissolution[59], cerussite precipitation[60,81] and/or ternary surface complexation
460 on ferric (oxyhydr)oxide precipitates[20].

461

462 ## 5. CONCLUSIONS

463 Siderite dissolution effectively removes 90% and 100% of initially 0.48 x10^{-3} mol kg^{-1} Pb(II)
464 from acidic oxic and anoxic aqueous solutions via three main pathways: neutralization, Pb-

carbonate formation and adsorption. Under either redox condition, the liberation of carbonate during siderite dissolution leads to rapid increase in reactive fluid pH. Simultaneously, Pb(II) rapidly precipitates as $PbCO_3$, which was identified by XRD, TEM and EXAFS as nanoparticulate cerussite. Additional XANES-mapping and XPS analyses confirmed Pb-carbonate formation on the siderite surface, which particularly controls Pb(II) consumption under anoxic conditions as well as during early stages of the reaction under oxic conditions. EXAFS shell-by-shell fitting showed that Pb(II) also readily forms inner-sphere Pb(II) adsorption complexes with the oxidation-induced goethite nanoprecipitates under oxic conditions, which dominates Pb(II) uptake from the oxic aqueous solution at a later stage of the reaction.

Overall, the nanoparticulate and scarcely soluble reaction products remained stable and no Pb was re-released over the entire experiment duration of 1008 h. Reduced conditions, however, allow faster and more stable capture of Pb(II) than oxic conditions due to cerussite formation. We further showed that the presence of Pb(II) does not affect the dissolution rate of the micro-granular natural siderite material, which remained governed by the reactive solution pH and its saturation state in the aqueous system. As a common iron ore (current market price \$103.30/t)[84], the material costs for siderite used as remediation reagent can be estimated assuming a reaction efficiency based on this study of 13.5 mg Pb sequestered per g siderite. Treatment of water contaminated with 100 mg L^{-1} aqueous Pb(II) using natural siderite would cost approximately \$0.69 per ton contaminated water, or \$2.00/t if using synthetic siderite[85]. This study thus demonstrates that natural siderite dissolution is an effective, low-cost and sustainable Pb(II) sequestration method for potential acidic wastewater remediation applications under either redox condition.

ASSOCIATED CONTENT

Supporting Information. The following files are available free of charge: 1) Supporting information on methodology, microscopic and spectroscopic results, and geochemical calculations (PDF). 2) Chemical solution data (MS Excel).

AUTHOR INFORMATION

Corresponding Authors

* Lisa C. Füllenbach. E-Mail: l.fuellenbach@ucl.ac.uk

* Eric H. Oelkers. E-Mail: e.oelkers@ucl.ac.uk

Author Contributions

The manuscript was written through contributions of all authors. All authors have given approval to the final version of the manuscript.

Notes

The authors declare no competing financial interest.

ACKNOWLEDGMENTS

This work was funded by the European Union's Horizon 2020 Marie Skłodowska-Curie Innovative Training Network Grant No. 675219. L.G. Benning acknowledges the financial support from the German Helmholtz Recruiting Initiative funding (award number I-044-16-01). Synchrotron mapping work was carried out with the support of the Diamond Light Source, instrument I14 (proposal MG21719-1). EXAFS work was conducted with the support of the ANKA-KIT, instrument SUL-X (proposal A2017-028-012253). Many thanks go to I. Wood for the XRD

506 analyses, to G. Saldi for providing BET measurements, to A. Schreiber for preparing FIB sections
507 for TEM, and to J. Stockmann (BAM) for performing the XPS measurements.

508 ABBREVIATIONS

509 Pb, lead; Pb O (LT), siderite dissolution experiment in Pb(II)-bearing solution under oxic
510 conditions (long-term); Pb A (LT), siderite dissolution experiment in Pb(II)-bearing solution under
511 anoxic conditions (long-term); ICP-OES, inductively coupled plasma optical emission
512 spectroscopy; SFA, segmented flow analysis; XRD, X-ray (powder) diffraction; (FE-)SEM, (field
513 emission) scanning electron microscopy; EDX, energy dispersive X-ray spectroscopy; FIB,
514 focused ion beam; (HR)TEM, (high-resolution) transmission electron microscopy; XAS, X-ray
515 absorption spectroscopy; XANES, X-ray absorption near edge structure; EXAFS, extended X-ray
516 absorption fine structure; XRF, X-ray fluorescence; XPS, X-ray photoelectron spectroscopy.

517 REFERENCES

518 (1) Lim, H.-S.; Lee; J.-S.; Chon, H.-T.; Sage, M. Heavy metal contamination and health risk
519 assessment in the vicinity of the abandoned Songcheon Au–Ag mine in Korea. *J. Geochem.*
520 *Exploration* ***2008****, 96*, 223–230; DOI 10.1016/j.gexplo.2007.04.008.

521 (2) Antoniadis, V.; Shaheen, S. M.; Boersch, J.; Frohne, T.; Laing, G. D.; Rinklebe, J.
522 Bioavailability and risk assessment of potentially toxic elements in garden edible vegetables and
523 soils around a highly contaminated former mining area in Germany. *J. Environ. Management*
524 ***2017****, 186*, 192–200; DOI 10.1016/j.jenvman.2016.04.036.

525 (3) Kasassi, A.; Ramkimbei, P.; Karagiannidis, A.; Zabaniotou, A.; Tsiouvaras, K.; Nastis, A.;
526 Tzafeiropoulou, K. Soil contamination by heavy metals: Measurements from a closed unlined
527 landfill. *Biores. Tech.* ***2008****, 99*, 8578–8584; DOI 10.1016/j.biortech.2008.04.010.

528 (4) Sun, C.; Liu, J.; Wang, Y.; Sun, L.; Yu, H. Multivariate and geostatistical analyses of the
529 spatial distribution and sources of heavy metals in agricultural soil in Dehui, Northeast China.
530 *Chemosphere* ***2013****, 92*, 517–523; DOI 10.1016/j.chemosphere.2013.02.063.

531 (5) Adamcová, D.; Radziemska, M.; Ridošková, A.; Bartoň, S.; Pelcová, P.; Ebl, J.; Kynický, J.;
532 Brtnický, M.; Vaverková, M. D. Environmental assessment of the effects of a municipal landfill
533 on the content and distribution of heavy metals in *Tanacetum vulgare* L. *Chemosphere* ***2017****, 185*,
534 1011–1018; DOI 10.1016/j.chemosphere.2017.07.060.

535 (6) Wong, K. K., Lee, C. K., Low, K. S., Haron, M. J. Removal of Cu and Pb from electroplating
536 wastewater using tartaric acid modified rice husk. *Process Biochem.* ***2003****, 39*, 437–445.

537 (7) Gäbler, H.-E.; Schneider, J. Assessment of heavy-metal contamination of floodplain soils
538 due to mining and mineral processing in the Harz Mountains, Germany. *Environ. Geol.* ***2000****, 39*
539 (7), 774–782.

540 (8) Chen, Y.; Liu, Y.; Liu, Y.; Lin, A.; Kong, Y.; Liu, D.; Li, X.; Zhang, Y.; Gao, Y.; Wang, D.
541 Mapping of Cu and Pb contaminations in soil using combined geochemistry, topography, and
542 remote sensing: A case study on the Le'an River floodplain, China. *Int. J. Environ. Res. Public*
543 *Health* ***2012****, 9*, 1874–1886; DOI 10.3390/ijerph9051874

(9) Pan, Y.; Li, H. Investigating heavy metal pollution in mining brownfield and its policy implications: A case study of the Bayan Obo Rare Earth Mine, Inner Mongolia, China. *Environ. Mgmt.* ***2016****, 57*, 879–893.

(10) Bargar, J. R.; Towle, S. N.; Brown, Jr., G. E.; Parks, G. A. Outer-sphere Pb(II) adsorbed at specific sites on single crystal α-alumina. *Geochim. Cosmochim. Acta* ***1996****, 60* (18), 3541–3547.

(11) Strawn, D. G.; Scheidegger, A. M.; Sparks, D. L. Kinetics and mechanisms of Pb(II) sorption and desorption at the aluminum oxide–water interface. *Environ. Sci. Tech.* ***1998****, 32,* 2596–2601.

(12) Strawn, D. G.; Sparks, D. L. The use of XAFS to distinguish between inner- and outer-sphere lead adsorption complexes on montmorillonite. *J. Colloid Interface Sci.* ***1999****, 216,* 257–269.

(13) Covelo, E. F.; Vega, F. A.; Andrade, M. L. Simultaneous sorption and desorption of Cd, Cr, Cu, Ni, Pb, and Zn in acid soils. I. Selectivity sequences. *J. Hazardous Mater.* ***2007****, 147,* 352–861.

(14) Davranche, M.; Bollinger, J.-C. Heavy metals desorption from synthesized and natural iron and manganese oxyhydroxides: Effect of reductive conditions. *J. Colloid Interface Sci.* ***2000****, 227*, 531–539; DOI 10.1006/jcis.2000.6904.

(15) Fulghum, J. E.; Bryan, S. R.; Linton, R. W. Discrimination between adsorption and coprecipitation in aquatic particle standards by surface analysis techniques: Lead distributions in calcium carbonates. *Environ. Sci. Tech.* ***1988****, 22,* 463–467.

564 (16) Rouff, A. A.; Reeder, R. J.; Fisher, N. S. Pb(II) sorption with calcite: A radiotracer study.
565 *Aquat. Geochem.* ***2002****, 8,* 203– 228.

566 (17) Elzinga, E. J.; Rouff, A. A.; Reeder, R. J. The long-term fate of Cu^{2+}, Zn^{2+}, and Pb^{2+}
567 adsorption complexes at the calcite surface: An X-ray absorption spectroscopy study. *Geochim.*
568 *Cosmochim. Acta* ***2006****, 70,* 2715–2725; DOI 10.1016/j.gca.2006.02.026.

569 (18) Gunneriusson, L.; Lövgren, L.; Sjöberg, S. Complexation of Pb(II) at the goethite (α-
570 FeOOH)/water interface: The influence of chloride. *Geochim. Cosmochim. Acta* ***1994****, 58* (22),
571 4973–4983.

572 (19) Ostergren, J. D.; Bargar, J. R.; Brown, Jr., G. E.; Parks, G. A. Combined EXAFS and FTIR
573 investigation of sulfate and carbonate effects on Pb(II) sorption to goethite (α-FeOOH). *J.*
574 *Synchrotron Rad.* ***1999****, 6,* 645–647. ISSN 0909-0495.

575 (20) Ostergren, J. D.; Trainor, T. P.; Bargar, J. R.; Brown, Jr., G. E.; Parks, G. A. Inorganic
576 ligand effects on Pb(II) sorption to goethite (α-FeOOH). I. Carbonate. *J. Colloid Interface Sci.*
577 ***2000****, 225,* 466-482; DOI 10.1006/jcis.1999.6701.

578 (21) Calmano, W.; Hong, J.; Förstner, U. Binding and mobilization of heavy metals in
579 contaminated sediments affected by pH and redox potential. *Wat. Sci. Tech.* ***1993****, 28* (8–9).

580 (22) Jensen, D. L.; Boddum, J. K.; Tjell, J. C.; Christensen, T. H. The solubility of rhodochrosite
581 ($MnCO_3$) and siderite ($FeCO_3$) in anaerobic aquatic environments. *Appl. Geochem.* ***2002****, 17,* 503–
582 511.

583 (23) Pedersen, H. D.; Postma, D.; Jakobsen, R. Release of arsenic associated with the reduction
584 and transformation of iron oxides. *Geochim. Cosmochim. Acta* ***2006****, 70,* 4116–4129; DOI
585 10.1016/j.gca.2006.06.1370.

586 (24) Nordstrom, D. K. Hydrogeochemical processes governing the origin, transport and fate of
587 major and trace elements from mine wastes and mineralized rock to surface waters. *Appl.*
588 *Geochem.* ***2011****, 26,* 1777–1791; DOI 10.1016/j.apgeochem.2011.06.002.

589 (25) Shaheen, S. M.; Rinklebe, J. Sugar beet factory lime affects the mobilization of Cd, Co, Cr,
590 Cu, Mo, Ni, Pb, and Zn under dynamic redox conditions in a contaminated floodplain soil. *J.*
591 *Environ. Management* ***2017****, 186,* 253–260; DOI 10.1016/j.envman.2016.07.060.

592 (26) Skousen, J. G.; Ziemkiewcz, P. F.; McDonald, L. M. Acid mine drainage formation, control
593 and treatment: Approaches and strategies. *Extractive Ind. Soc.* ***2019****, 6,* 241-249; DOI
594 10.1016/j.exis.2018.09.008.

595 (27) Erdem, M.; Gür, F.; Tümen, F. Cr(VI) reduction in aqueous solutions by siderite. *J.*
596 *Hazardous Mater. B113* ***2004****,* 217–222; DOI 10.1016/j.jhazmat.2004.06.012.

597 (28) Tang, Y.; Martin, S. T. Siderite dissolution in the presence of chromate. *Geochim.*
598 *Cosmochim. Acta* ***2011****, 75,* 4951–4962. DOI 10.1016/j.gca.2011.06.024.

599 (29) Bibi, I.; Niazi, N. K.; Choppala, G.; Burton, E. D. Chromium(VI) removal by siderite
600 ($FeCO_3$) in anoxic aqueous solutions: An X-ray absorption spectroscopy investigation. *Sci. Total*
601 *Environ.* ***2018****, 640–641,* 1424–1431; DOI 10.1016/j.scitotenv.2018.06.003.

(30) Jönsson, J.; Sherman, D. M. Sorption of As(III) and As(V) to siderite, green rust (fugerite) and magnetite: Implications for arsenic release in anoxic groundwaters. *Chem. Geol.* ***2008****, 255,* 173–181; DOI 10.1016/j.chemgeo.2008.06.036.

(31) Renard, F.; Putnis, C. V.; Montes–Hernandez, G.; King, H. E. Siderite dissolution coupled to iron oxyhydroxide precipitation in the presence of arsenic revealed by nanoscale imaging. *Chem. Geol.* ***2017****, 449,* 123–134; DOI 10.1016/j.chemgeo.2016.12.001.

(32) Ha, J.; Zhao, X.; Yu, R.; Barkay, T.; Yee, N. Hg(II) reduction by siderite ($FeCO_3$). *Appl. Geochem.* ***2017****, 78,* 211–218; DOI 10.1016/j.apgeochem.2016.12.017.

(33) Bénézeth, P.; Dandurand, J. L.; Harrichoury, J. L. Solubility product of siderite ($FeCO_3$) as a function of temperature (25–250 °C). *Chem. Geol.* ***2009****, 265,* 3–12; DOI 10.1016/j.chemgeo.2009.03.015.

(34) Duckworth, O. W.; Martin, S. T. Dissolution rates and pit morphology of rhombohedral carbonate minerals. *Am. Mineral.* ***2004****, 89,* 554–563.

(35) Stookey, L. L. Ferrozine – A new spectrophotometric reagent for iron. *Anal. Chem.* ***1970****, 42* (7), 779–781.

(36) Ravel, B.; Newville, M. ATHENA, ARTEMIS, HEPHAESTUS: data analysis for X-ray absorption spectroscopy using IFEFFIT. *J. Synchrotron Rad.* ***2005****, 12,* 537–541; DOI 10.1107/S090904950512719.

(37) Hesse, R.; Bundesmann, C.; Denecke, R. Automatic spike correction using UNIFIT 2020. *Surf. Interface Anal.* ***2019****, 51,* 1342–1350.

(38) Parkhurst, D. L.; Appelo, C. A. J. Description of input and examples for PHREEQC version 3 – A computer program for speciation, batch-reaction, one-dimensional transport, and inverse geochemical calculations. In *U.S. Geological Survey Techniques and methods, book 6*; U.S. Geological Survey: Denver, Colorado 2013; p. 1–497.

(39) Morgan, B.; Lahav, O. The effect of pH on the kinetics of spontaneous Fe(II) oxidation by O_2 in aqueous solution – basic principles and a simple heuristic description. *Chemosphere* ***2007****, 68*, 2080–2084.

(40) *European Union Council Directive 98/83/EC. On the quality of water intended for human consumption OJ L 330. 1998L0083-EN-07.10.2015;* Commission Directive (EU) 2015/1787; The Council of the European Union: Brussels, 2015; https://eur-lex.europa.eu/legal-content/EN/TXT/PDF/?uri=CELEX:01998L0083-20151027&from=EN

(41) Wehrli, B.; Sulzberger, B.; Stumm, W. Redox processes catalyzed by hydrous oxide surfaces. *Chem. Geol.* ***1989****, 78*, 167–179.

(42) Stumm, W.; Sulzberger, B. The cycling of iron in natural environments: Considerations based on laboratory studies of heterogeneous redox processes. *Geochim. Cosmochim. Acta* ***1992****, 56*, 3233–3257.

(43) Pedersen, H. D.; Postma, D.; Jakobsen, R. Release of arsenic associated with the reduction and transformation of iron oxides. *Geochim. Cosmochim. Acta* ***2006****, 70,* 4116–4129; DOI 10.1016/j.gca.2006.06.1370.

641 (44) Bargar, J. R.; Brown, Jr., G. E.; Parks, G. A. Surface complexation of Pb(II) at oxide–water
642 interfaces: II. XAFS and bond-valence determination of mononuclear Pb(II) sorption products and
643 surface functional groups on iron oxides. *Geochim. Cosmochim. Acta* ***1997****, 61* (13), 2639–2652.

644 (45) Bargar, J. R.; Brown, Jr., G. E.; Parks, G. A. Surface complexation of Pb(II) at oxide-water
645 interfaces: III. XAFS determination of Pb(II) and Pb(II)-chloro adsorption complexes on goethite
646 and alumina. *Geochim. Cosmochim. Acta* ***1998****, 62* (2), 193–207.

647 (46) Trivedi, P.; Dyer, J. A.; Sparks, D. L. Lead sorption onto ferrihydrite. 1. A Macroscopic
648 and spectroscopic assessment. *Environ. Sci. Tech.* ***2003****, 37* (5)*,* 908–914; DOI
649 10.1021/es.0257927.

650 (47) Liu, H.; Lu, X.; Li, M.; Zhang, L.; Pan, C.; Zhang, R.; Li, J.; Xiang, W. Structural
651 incorporation of manganese into goethite and its enhancement of Pb(II) adsorption. *Environ. Sci.*
652 *Tech.* ***2018****, 52,* 4719–4727; DOI 10.1021/acs.est.7b05612.

653 (48) Newville, M. Fundamentals of XAFS. *Rev. Min. Geochem.* ***2014****, 78,* 33–74. DOI
654 10.2138/rmg.2014.78.2.

655 (49) Chevrier, G.; Giester, G.; Heger, G.; Jarosch, D.; Wildner, M.; Zemann, J. Neutron single-
656 crystal refinement of cerussite, $PbCO_3$, and comparison with other aragonite-type carbonates. *Zeit.*
657 *Krist.* ***1992****, 199,* 67–74.

658 (50) Pederson, L. R. Two-dimensional chemical state plot for lead using XPS. *J. Electron Spectr.*
659 *Rel. Phen.* ***1982****, 28,* 203–209.

660 (51) Feng, Q.; Wen, S.; Zhao, W.; Deng, J.; Xian, Y. Adsorption of sulfide ions on the cerussite
661 surfaces and implications for floatation. *Appl. Surf. Sci.* ***2016****, 360,* 365–372; DOI
662 10.1016/j.apsus.2015.11.035

663 (52) Godelitsas, A.; Astilleros, J. M.; Hallam, K.; Harissopoulos, S.; Putnis, A. Interaction of
664 calcium carbonates with lead in aqueous solutions. *Environ. Sci. Tech.* ***2003****, 37,* 3351–3360; DOI
665 10.1021/es020238i.

666 (53) Stipp, S. L.; Hochella, Jr., M. F. Structure and binding environments at the surface as
667 observed with X-ray photoelectron spectroscopy (XPS) and low energy electron diffraction
668 (LEED). *Geochim. Cosmochim. Acta* ***1991****, 55*, 1723–1736.

669 (54) Duckworth, O. W.; Martin, S. T. Role of molecular oxygen in the dissolution of siderite and
670 rhodochrosite. *Geochim. Cosmochim. Acta* ***2004****, 68* (3), 607–621.

671 (55) Golubev, S. V.; Bénézeth, P.; Schott, J.; Dandurand, J. L.; Castillo, A. Siderite dissolution
672 kinetics in acidic aqueous solutions from 25 to 100 °C and 0 to 50 atm pCO_2. *Chem. Geol.* ***2009****,*
673 *265,* 13–19; DOI 10.1016/j.chemgeo.2008.12.031.

674 (56) Renard, F.; Røyne, A.; Putnis, C. V. Timescale of interface-coupled dissolution-
675 precipitation reactions on carbonates. *Geosci. Front.* ***2019****, 10,* 17–27; DOI
676 10.1016/j.gsf.2018.02.013.

677 (57) Kleber, W.; Bautsch, H.-J.; Bohm, J. *Einführung in die Kristallographie*, 19th ed.;
678 Oldenbourg Verlag: München, 2010.

679 (58) Cubillas, P.; Köhler, S.; Prieto, M.; Causserand, C.; Oelkers, E. H. How do mineral coatings
680 affect dissolution rates? An experimental study of coupled $CaCO_3$ dissolution–$CdCO_3$

681 precipitation. *Geochim. Cosmochim. Acta* ***2005****, 69* (23), 5459–5476; DOI
682 10.1016/j.gca.2005.07.016.

683 (59) Bruno, J.; Wersin, P.; Stumm, W. On the influence of carbonate in mineral dissolution: II.
684 The solubility of $FeCO_3$(s) at 25 ºC and 1 atm total pressure. *Geochim. Cosmochim. Acta* ***1992****,*
685 *56*, 1149–1155.

686 (60) Bilinski, H.; Schindler, P. Solubility and equilibrium constants of lead in carbonate solutions
687 (25 °C, I = 0.3 mol dm^{-3}). *Geochim. Cosmochim. Acta* ***1982****, 46,* 921–928.

688 (61) Grauer, R. Solubility products of M(II)-carbonates. PSI: Bericht No. 99-04. ISSN 1019-
689 0643.

690 (62) Shannon, R. D. Revised effective ionic radii and systematic studies of interatomic distances
691 in halides and chalcogenides. *Acta Cryst.* ***1976****, A 32,* 751–767.

692 (63) Effenberger, H.; Mereiter, K.; Zemann, J. Crystal structure refinements of magnesite,
693 calcite, rhodochrosite, siderite, smithsonite, and dolomite, with discussion of some aspects of the
694 stereochemistry of calcite type carbonates. *Zeit. Krist.* ***1981****, 156,* 233–243.

695 (64) Reeder, R. J.; Lamble, G. M.; Northrup, P.A. XAFS study of the coordination and local
696 relaxation around Co^{2+}, Zn^{2+}, Pb^{2+}, and Ba^{2+} trace elements in calcite. *Am. Mineral.* ***1999****, 84,*
697 1048–1060.

698 (65) Callagon, E.; Fenter, P.; Nagy, K. L.; Sturchio, N. C. Incorporation of Pb at the calcite
699 (104)–water interface. *Environ. Sci. Technol.* ***2014****, 48*, 9263–9269.

(66) Rouff, A. A.; Elzinga, E. J.; Reeder, R. J.; Fisher, N. S. X-ray absorption spectroscopic evidence for the formation of Pb(II) inner-sphere adsorption complexes and precipitates at the calcite–water interface. *Environ. Sci. Tech.* ***2004****, 38,* 1700–1707.

(67) Rouff, A. A.; Elzinga, E. J.; Reeder, R. J.; Fisher, N. S. The influence of pH on the kinetics, reversibility and mechanisms of Pb(II) sorption at the calcite–water interface. *Geochim. Cosmochim. Acta* ***2005****, 69* (22), 5173–5186.

(68) Stipp, S. L.; Hochella, Jr., M. F.; Parks, G. A.; Leckie, J. O. Cd^{2+} uptake by calcite, solid-state diffusion, and the formation of solid-solution: Interface processes observed with near-surface sensitive techniques (XPS, LEED, and AES). *Geochim. Cosmochim. Acta* ***1992****, 56,* 1941–1954.

(69) Prieto, M.; Cubillas, P.; Fernández-Gonzalez, Á. Uptake of dissolved Cd by biogenic and abiogenic aragonite: a comparison with sorption onto calcite. *Geochim. Cosmochim. Acta* ***2003****, 67* (20), 3859–3869.

(70) Köhler, S. J.; Cubillas, P.; Rodríguez-Blanco, J. D.; Bauer, C.; Prieto, M. Removal of cadmium from wastewaters by aragonite shells and the influence of other divalent cations. *Environ. Sci. Technol.* ***2007****, 41*, 112–118.

(71) Yuan, K., Lee, S. S., De Andrade, V.; Sturchio, N. C.; Fenter, P. Replacement of calcite ($CaCO_3$) by cerussite ($PbCO_3$). *Environ. Sci. Tech.* ***2016****, 50,* 12984–12991; DOI 10.1021/acs.est.6b03911.

(72) Di Lorenzo, F.; Cametti, G.; Vanhecke, D.; Churakov, S. V. The role of interfaces in controlling Pb^{2+} removal by calcium carbonate minerals. *Cryst. Growth Des.* ***2020****, 20*, 6157–6169.

(73) Hill, R. J. Refinement of the structure of orthorhombic PbO (massicot) by rietveld analysis of neutron powder diffraction data. *Acta Cryst.* ***1985****, C41*, 1281–1284.

(74) Bargar, J.R.; Brown Jr, G. E.; Parks, G. A. Surface complexation of Pb(II) at oxide–water interfaces: I. XAFS and bond-valence determination of mononuclear and polynuclear Pb(II) sorption products on aluminum oxides. *Geochim. Cosmochim. Acta* ***1997****, 61* (13), 2617–2637.

(75) Erdem, M.; Özverdi, A. Lead adsorption from aqueous solution onto siderite. *Sep. Purif. Tech.* ***2005****, 42,* 259–264; DOI 10.1016/j.seppur.2004.08.004.

(76) Zachara, J. M.; Kittrick, J. A.; Harsh, J. B. The mechanism of Zn^{2+} adsorption on calcite. *Geochim. Cosmochim. Acta* ***1988****, 52,* 2281–2291.

(77) Charlet, L.; Wersin, P.; Stumm, W. Surface charge of $MnCO_3$ and $FeCO_3$. *Geochim. Cosmochim. Acta Lett.* ***1990****, 54,* 2329–2336.

(78) Van Capellen, P.; Charlet, L.; Stumm, W.; Wersin, P. A surface complexation model of the carbonate mineral-aqueous solution interface. *Geochim. Cosmochim. Acta* ***1993****, 57,* 3505–3518.

(79) Hsu, P. H.; Marion, G. The solubility product of goethite. *Soil Sci.* ***1985****, 140* (5), 344–351.

(80) Zinder, B.; Furrer, G.; Stumm, W. The coordination chemistry of weathering: II. Dissolution of Fe(III) oxides. *Geochim. Cosmochim. Acta* ***1986****, 50,* 1861–1869.

(81) Taylor, P.; Lopata, V. J. Stability and solubility relationships between some solids in the system $PbO–CO_2–H_2O$. *Can. J. Chem.* ***1984****, 62,* 395–402.

738 (82) Gilbert, B.; Ono, R. K.; Ching, K. A.; Kim, C. S. The effects of nanoparticle aggregation
739 processes on aggregate structure and metal uptake. *J. Colloid Interface Sci.* ***2009****, 339,* 285–295;
740 DOI 10.1016/j.jcis.2009.07.058.

741 (83) Stegemeier, J. P.; Reinsch, B. C.; Lentini, C. J.; Dale, J. G.; Kim, C. S. Aggregation of
742 nanoscale iron oxyhydroxides and corresponding effects on metal uptake, retention, and
743 speciation: II. Temperature and time. *Geochim. Cosmochim. Acta* ***2015****, 148,* 113–129.

744 (84) Tuck, C. C.; Phamdag, H. P. Mineral industry survey. Iron Ore in June 2020. *USGS,*
745 *September* ***2020****. https://www.usgs.gov/centers/nmic/iron-ore-statistics-and-information.*

746 (85) Guo, H.; Li, Y.; Zhao, K.; Ren, Y.; Wei, C. Removal of arsenite from water by synthetic
747 siderite: Behaviors and mechanisms. *J. Haz. Mater.* ***2011****, 186*, 1847–1854.

748

749 GRAPHICAL ABSTRACT.

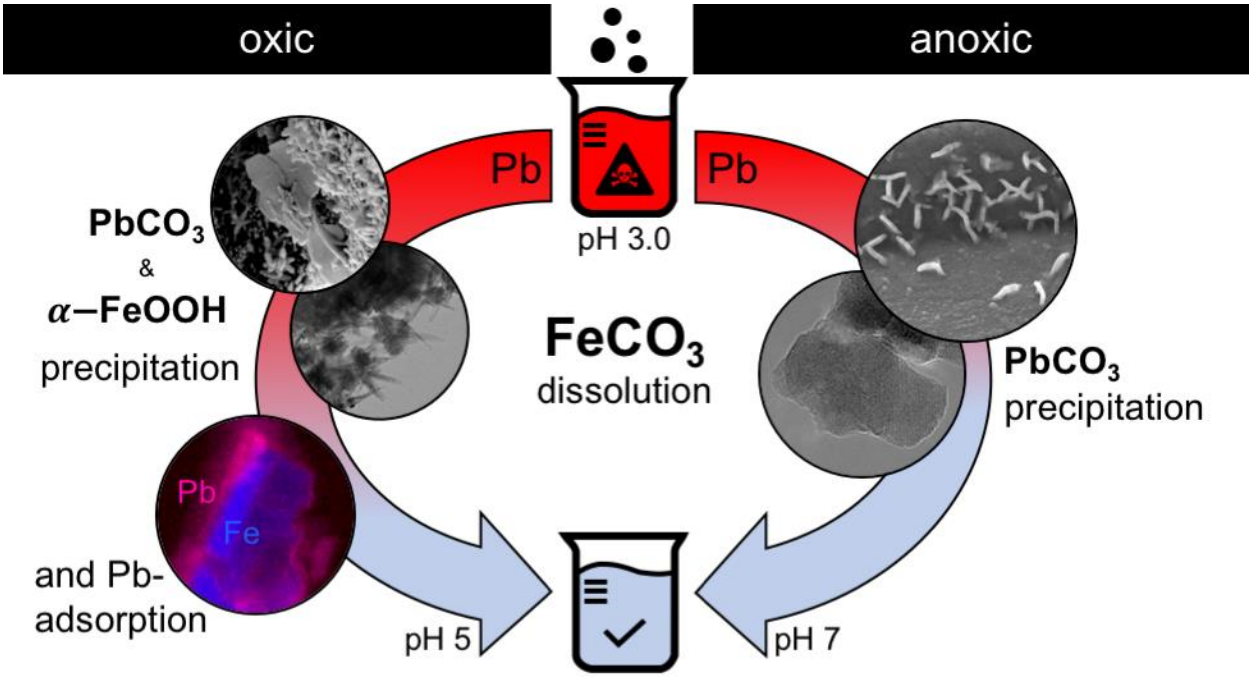

750

751 For Table of Contents Only.